



Rotavirus VP4 Epitope of a Broadly Neutralizing Human Antibody Defined by Its Structure Bound with an Attenuated-Strain Virion

Simon Jenni,^a Zongli Li,^{a,b} Yuhuan Wang,^c Theresa Bessey,^c Eric N. Salgado,^{d*} Aaron G. Schmidt,^{e,f} Harry B. Greenberg,^{g,hi} Baoming Jiang,^c Stephen C. Harrison^{a,b,d}

^aDepartment of Biological Chemistry and Molecular Pharmacology, Harvard Medical School, Boston, Massachusetts, USA

^bHoward Hughes Medical Institute, Harvard Medical School, Boston, Massachusetts, USA

^cDivision of Viral Diseases, Centers for Disease Control and Prevention, Atlanta, Georgia, USA

^dLaboratory of Molecular Medicine, Boston Children's Hospital, Boston, Massachusetts, USA

^eRagon Institute of MGH, MIT, and Harvard, Cambridge, Massachusetts, USA

^fHarvard Medical School, Boston, Massachusetts, USA

^gDepartment of Medicine, Stanford University School of Medicine, Stanford, California, USA

^hDepartment of Microbiology and Immunology, Stanford University School of Medicine, Stanford, California, USA

ⁱVA Palo Alto Health Care System, Palo Alto, California, USA

Simon Jenni and Zongli Li contributed equally to this article. Author order was determined by discussion and mutual agreement.

ABSTRACT Rotavirus live-attenuated vaccines, both mono- and pentavalent, generate broadly heterotypic protection. B-cells isolated from adults encode neutralizing antibodies, some with affinity for VP5*, that afford broad protection in mice. We have mapped the epitope of one such antibody by determining the high-resolution cryo-EM structure of its antigen-binding fragment (Fab) bound to the virion of a candidate vaccine strain, CDC-9. The Fab contacts both the distal end of a VP5* β -barrel domain and the two VP8* lectin-like domains at the tip of a projecting spike. Its interactions with VP8* do not impinge on the likely receptor-binding site, suggesting that the mechanism of neutralization is at a step subsequent to initial attachment. We also examined structures of CDC-9 virions from two different stages of serial passaging. Nearly all the VP4 (cleaved to VP8*/VP5*) spikes on particles from the earlier passage (wild-type isolate) had transitioned from the “upright” conformation present on fully infectious virions to the “reversed” conformation that is probably the end state of membrane insertion, unable to mediate penetration, consistent with the very low *in vitro* infectivity of the wild-type isolate. About half the VP4 spikes were upright on particles from the later passage, which had recovered substantial *in vitro* infectivity but had acquired an attenuated phenotype in neonatal rats. A mutation in VP4 that occurred during passaging appears to stabilize the interface at the apex of the spike and could account for the greater stability of the upright spikes on the late-passage, attenuated isolate.

IMPORTANCE Rotavirus live-attenuated vaccines generate broadly heterotypic protection, and B-cells isolated from adults encode antibodies that are broadly protective in mice. Determining the structural and mechanistic basis of broad protection can contribute to understanding the current limitations of vaccine efficacy in developing countries. The structure of an attenuated human rotavirus isolate (CDC-9) bound with the Fab fragment of a broadly heterotypic protective antibody shows that protection is probably due to inhibition of the conformational transition in the viral spike protein (VP4) critical for viral penetration, rather than to inhibition of receptor binding. A comparison of structures of CDC-9 virus particles at two stages of serial passaging supports a proposed mechanism for initial steps in rotavirus membrane penetration.

Editor Stacey Schultz-Cherry, St. Jude Children's Research Hospital

This is a work of the U.S. Government and is not subject to copyright protection in the United States. Foreign copyrights may apply.

Address correspondence to Harry B. Greenberg, hbgreen@stanford.edu, Baoming Jiang, bxj4@cdc.gov, or Stephen C. Harrison, harrison@crystal.harvard.edu.

*Present address: Eric N. Salgado, Pfizer Inc., Cambridge, Massachusetts, USA.

The authors declare no conflict of interest.

Received 24 April 2022

Accepted 1 July 2022

Published 4 August 2022

KEYWORDS cryo-EM, rotavirus structure, vaccine strain

The two most widely licensed rotavirus vaccines have substantially lower efficacy in developing countries than in the US, motivating efforts to seek additional vaccine candidates (1, 2). CDC-9 is a potential vaccine strain generated at the Center for Disease Control and Prevention (CDC) by serial passaging of virus isolated from the stool of an infected donor (3, 4). Seven passages in MA104 cells followed by 38 in Vero cells yielded a strain with 10 amino acid mutations, 6 in VP4 and the rest distributed one each in VP1, VP6, NSP1, and NSP5, and a deletion of 10 residues in VP2 (Table 1 in Ref. 4). In the Caco-2 human cell line, the Vero cell-adapted, passage 44/45 (P45) virus grew to titers two logs greater than did the original isolate in MA104 cells but had a substantially attenuated response in neonatal rats, consistent with findings for many viruses for which extended serial passaging has led to attenuation in an animal host.

The epitopes of protective, neutralizing antibodies that any effective vaccine should elicit are on the two outer-layer rotavirus proteins, VP4 and VP7 (see Fig. 1A for an illustration of rotavirus structural proteins and for the definition of double-layer and triple-layer particles [DLPs and TLPs, respectively]). When a rotavirus particle encounters a cell, the VP4 “spike” protein, activated by trypsin cleavage to VP8* and VP5*, mediates both attachment and penetration. The latter event requires perforation of the plasma membrane that surrounds the endocytosed virion followed by dissociation of VP7 and VP8*/VP5* and release of the DLP into the cytosol (5–7). Transition from the upright, asymmetric VP8*/VP5* spike present on a mature TLP to a reversed, 3-fold symmetric structure is an essential molecular step in this sequence of events (Fig. 1). Cryogenic electron microscopy (cryo-EM) of rhesus rotavirus particles attached to liposomes has shown that the “foot” domain of VP5*, which anchors it on the TLP surface, unfolds, projects outwards, and inserts into a membrane of the target cell (8). This interaction appears to be a key event in membrane perforation.

The antigenic diversity of human rotaviruses includes a combination of a various P (VP4) and G (VP7) serotypes (Data set S1–S3 in the supplemental material). Nonetheless, the two most widely licensed vaccines worldwide, mono- and pentavalent, respectively, both yield substantial protection against most heterologous human RV strains (9), consistent with data on protection by natural infection (10). In keeping with these findings, isolation of human intestinal, IgA-secreting B cells from adult donors, using CDC-9 TLPs for sorting, showed that a subset of immunoglobulins (Igs), elicited originally by natural (monospecific) infection, could mediate heterotypic protection in mice (11). Most of the heterotypically reactive/neutralizing antibodies appeared to recognize epitopes on VP5*. Thus, monotypic exposure, from either vaccination or infection, yields heterotypic immunity that substantially reduces severe symptomatic illness from multiple rotavirus serotypes.

We report here a full description of the epitope of one such broadly heterotypic, neutralizing antibody, from the structure, determined by cryo-EM, of a TLP with the Fab41 (neutralizing MAb #41) (11). We show that the epitope of MAb #41, originally described as VP5* directed, includes residues on both VP8* lectin domains and one VP5* β -barrel domain. Although the antibody footprint does not overlap known receptor binding sites and probably does not block attachment, it is likely to lock the spike into its upright conformation on the mature TLP and prevent the transition to the reversed conformation, thereby inhibiting penetration. The results also offer explanations for the very poor infectivity in cell culture of the unmutated wild-type isolate and for the enhancement of *in vitro* infectivity that resulted from mutations selected during serial passage.

RESULTS

Spike conformations and model building. We recorded cryo-EM images of the CDC-9 P12 and P45 preparations, the latter with Fab41 added, on a TF30 Polara microscope operated at 300 kV and equipped with a Gatan K2 detector. Classification in 2D showed that the P45 particles (two data sets collected from two virus preparations) were

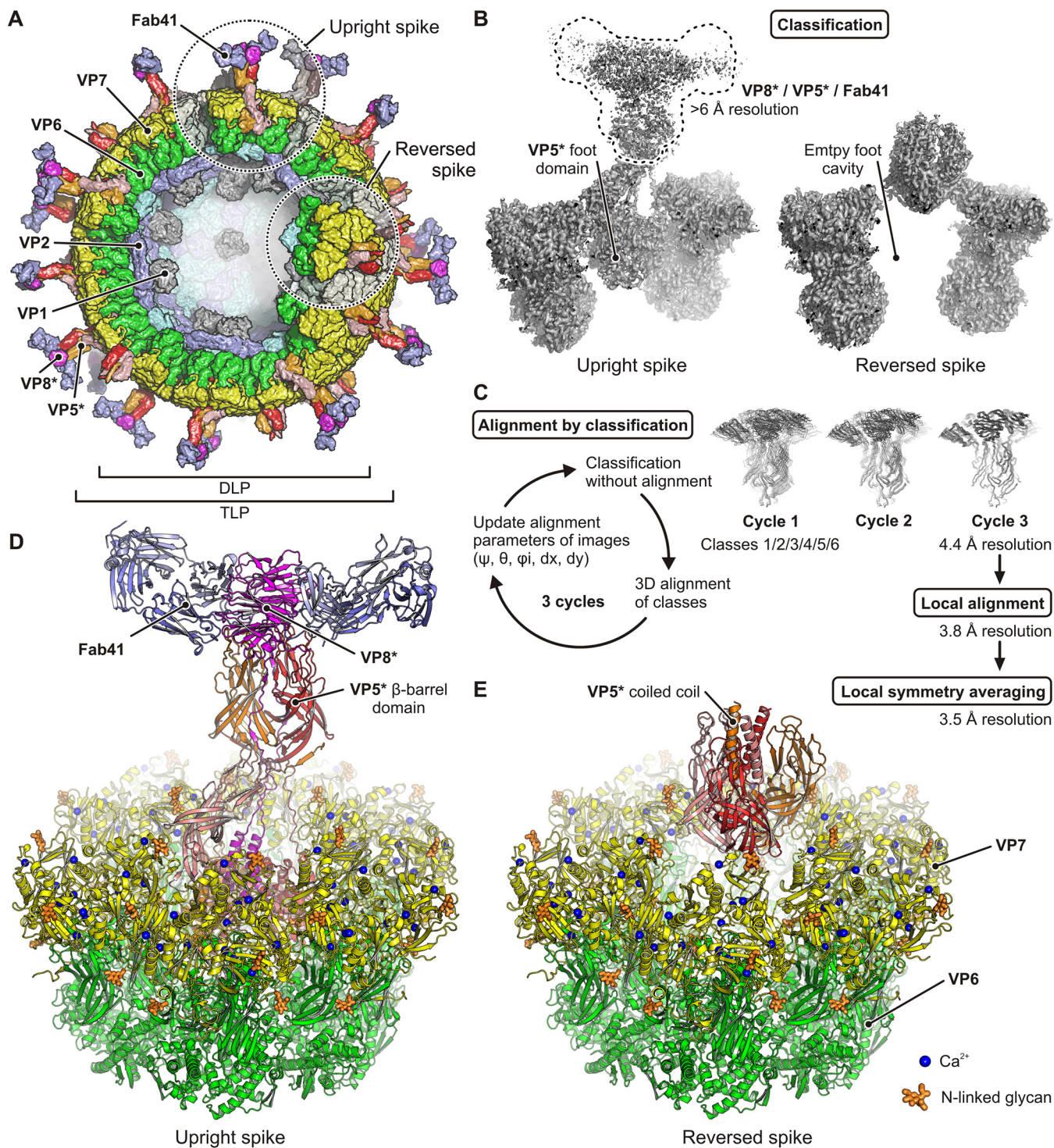


FIG 1 Upright and reversed spike protein conformations on human rotavirus strain CDC-9 passage 45 (P45). (A) Architecture of the rotavirus triple-layer particle (TLP). The capsid shell protein VP2 (cyan and blue) encapsidates the double stranded-RNA genomic segments (not shown), capping enzymes (VP3, not shown), and RNA-dependent RNA polymerases (VP1, gray). The VP2 and VP6 (green) layers, together with their VP1, VP3 and dsRNA-genome contents, constitute a double-layer particle (DLP). VP7 (yellow) forms an outer layer that anchors the VP4 spike protein, which is cleaved by trypsin into VP8* (magenta) and VP5* (red, orange, salmon). Spikes are shown in upright and reversed conformations on the virus particle. Fab41 antibodies bound to upright spikes are shown in blue. (B) cryo-EM reconstructions of the upright (left) and reversed (right) spike conformations obtained by subparticle classification. A dashed line surrounds the region in the upright conformation map, consisting of distal spike components that were subjected to focused reconstruction. (C) Focused reconstruction of distal spike components using alignment by classification, local alignment, and local symmetry averaging. See Methods for details. (D) Structure of the upright spike conformation with bound Fab41 antibodies. (E) Structure of the reversed spike conformation.

TABLE 1 Human rotavirus strain CDC-9 P12 and P45 classification results

Classification	P12	P45 (data set 1)	P45 (data set 2)
Whole virus classification			
No. of particles	5612	9871	6823
“Triple-layer” particle (%)	40.6	96.6	97.6
“Double-layer” particle (%)	59.4	3.4	2.4
Spike classification			
No. of particles ^a	336720	592260	409380
Upright conformation (%)	N.o. ^b	37.2	47.1
Intermediate conformation (%)	31.8	N.o.	N.o.
Reversed conformation (%)	50.6	62.8	43.8
Unoccupied (no VP8*/VP5*) (%)	17.6	N.o.	9.2

^aSixty spike subparticles per whole virus.

^bN.o., not observed.

nearly all TLPs but that about 60% of the particles in the P12 preparation were DLPs (Fig. S1 in the supplemental material and Table 1). We computed 3D reconstructions of the P12 and P45 TLPs, initially with icosahedral symmetry. Inspection of the regions around the VP4 spike suggested a superposition of two conformations – the upright spike seen on mature TLPs and a reversed VP5* trimer, which appears spontaneously but slowly on rhesus rotavirus (RRV) TLPs at near-neutral pH and 37°C, and rapidly at pH >10.5 (8). After icosahedral alignment, we extracted subparticles corresponding to each of the 60 VP4 spikes from all the TLP particles in the stack, after subtracting from each particle image the projected signal from the rest of the reference structure, except for the two bound Fabs, VP5*/VP8*, and one of the six VP7 trimers surrounding the spike in question. Subparticle reconstruction, followed by subparticle classification without alignment, yielded three classes for each preparation, even after allowing for additional classes (Table 1). In the P12 preparation, about 50% of the spikes were in the reversed conformation, 32% in a conformation with the foot domain still in place but with no clear density for the 2-fold clustered projecting VP5* β -barrel domains and their associated VP8* lectin domains; about 18% of the spike positions were empty. In the P45 preparation, the upright and reversed conformations each accounted for about 45% of the VP4 trimers, and about 10% of the positions were empty. Only the upright spikes on the P45 particles had bound Fabs—one for each of the two outward projecting subunits. Except for small differences accounted for by differences in amino-acid sequence, the reversed spike structures on particles from both the P12 and P45 preparations were essentially identical to the reversed VP5* structure we have described for RRV (8) (Fig. 1E).

The initial spike:Fab subparticle reconstruction had poor resolution (>6 Å) for the projecting VP5* β -barrel domains, their associated VP8* lectin domains, and the Fabs (Fig. 1B and Fig. S2 in the supplemental material). Further classification (without alignment) into six classes of sub-particles tightly masked around these features showed that they pivot over a range of several degrees about their contact with the tip of the third VP5* β -barrel domain (Fig. 1B and C). We therefore superposed the densities for all six classes and combined them into a single reference for aligning the six tightly masked regions, leading to a map at 3.8 Å resolution that could be further sharpened to about 3.5 Å by averaging its two identical halves (Fig. S2).

We built a model of the Fab complex as described in Methods. We built the Fab41 as a homology model based on the crystal structures of antibodies closest in sequence (heavy chain PDB-ID 6PHC with 87% sequence identity, light chain PDB-ID 6MG4 with 91% sequence identity), then adjusted it to fit the map (Fig. S3 in the supplemental material). The VP4, VP7, and VP6 components could be fit by straightforward modification of the subunit structures from the RRV TLPs (8, 12) (Fig. 1D and E). We found four Ca²⁺ ions per VP7 protomer, two of which are coordinated by residues from different VP7 protomers. They stabilize the outer layer of the particle, and uncoating requires their dissociation (13). The interface between antibody variable domains and VP4 was

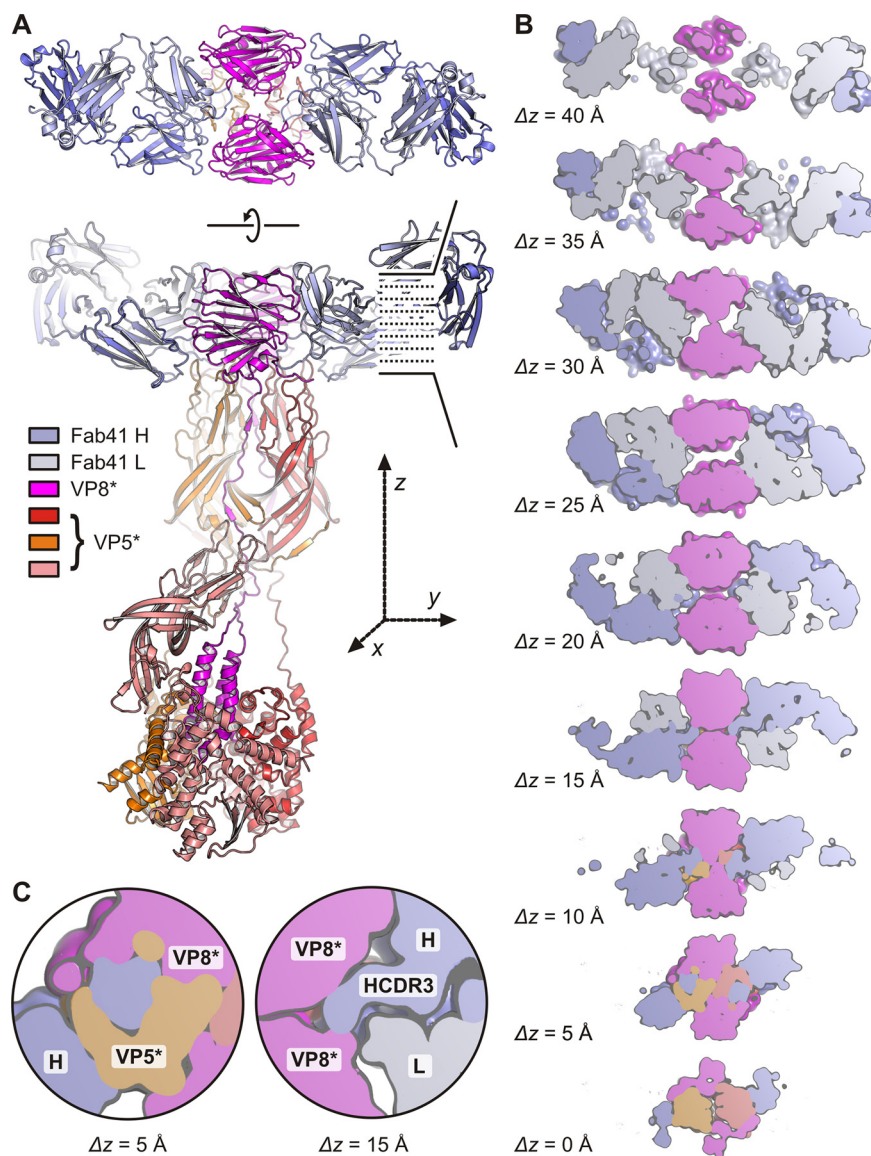


FIG 2 Structure of the upright VP8*/VP5* spike in complex with the Fab of neutralizing antibody 41. (A) Overview of the upright spike structure with two Fab41 antibodies bound at the apex. VP8* is colored magenta and the three VP5* chains are colored red, orange and salmon, respectively. The Fab41 heavy and light chains are colored blue and gray, respectively. (B) Sequential cross sections of the antibody binding site along the axis indicated by z. The relative positions along the axis are given in Angstrom. Domains are colored as in (A). (C) Close-up views of two cross sections, showing heavy chain contacts to both VP8* and VP5* (left), and the HCDR3 inserted between the two VP8* domains (right).

sufficiently well defined that we could describe specific contacts, as outlined in the following section.

VP4:Fab41 contacts. The antibody binds at the VP5*–VP8* junction, well displaced from the likely receptor site (Fig. 2). It contacts one VP5* and both VP8*s, apparently locking those components in place, as also suggested by the sharp density features for the VP8* lectin domain and for the link connecting it with the VP8* N-terminal helix. A footprint of the antibody contacts mapped on the VP5*–VP8* spike structure shows that the Fab41 heavy chain binds to the VP5* β -barrel domain and to one of the two VP8* domains. The Fab41 light chain binds the other VP8* domain (Fig. 3A). Mapping residue conservation from a VP4 multiple sequence alignment of different rotavirus strains (data set S1) onto the molecular surface shows patches of conserved residues

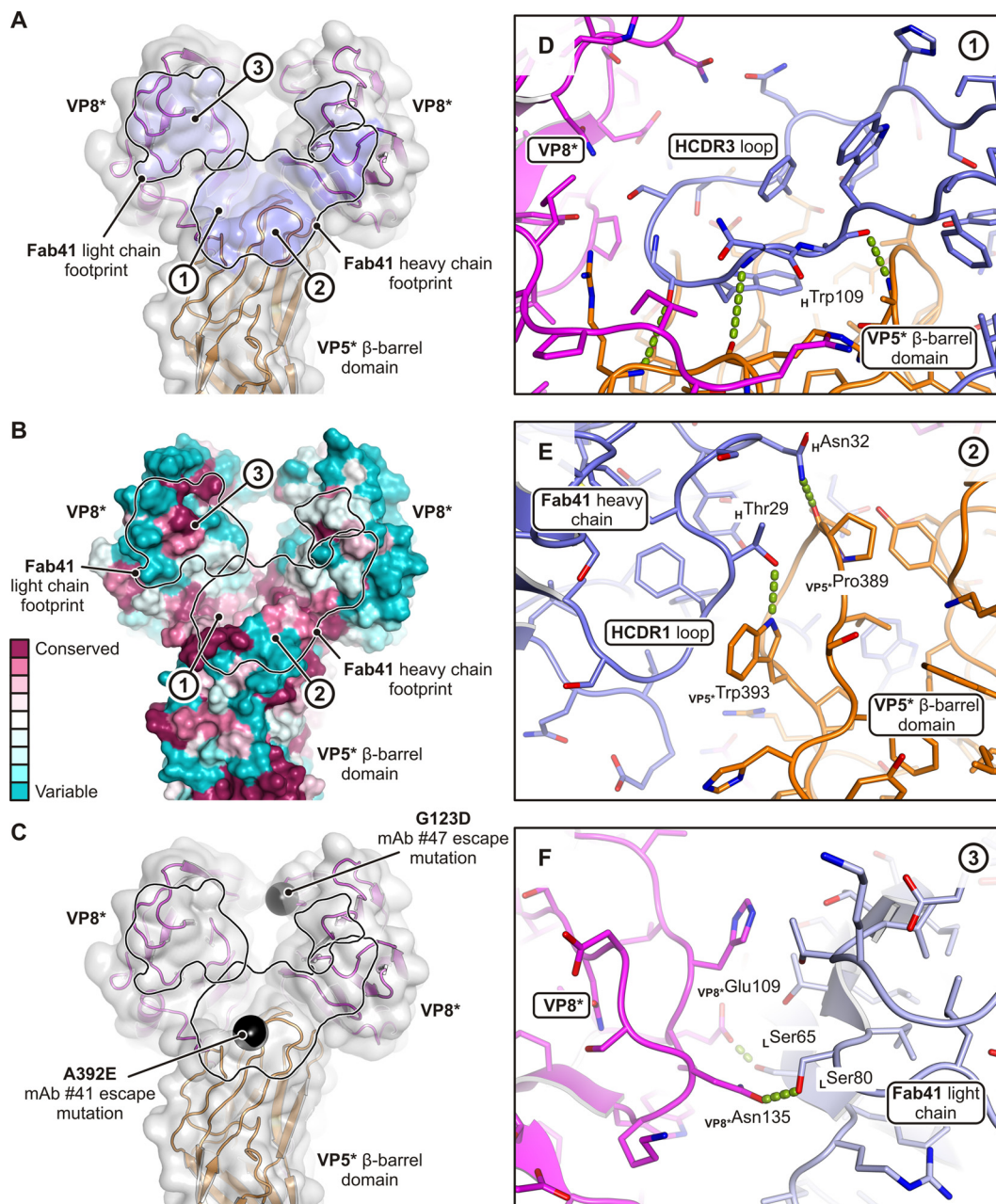


FIG 3 The Fab41-VP5*/VP8* antibody-antigen interface. (A) The VP8*/VP5* spike apex is shown in ribbon representation enclosed by a transparent surface. The bound Fab41 antibody is omitted to allow direct view of its epitope. The footprints of the heavy (blue) and light (light blue) chains on VP8*/VP5* are indicated by black lines. The numbers 1–3 refer to critical regions of the antibody-antigen binding interface, for which corresponding panels D–F show details. (B) Surface residue conservation of VP5*/VP8*. Conservation scores were calculated from the VP4 multiple sequence alignment (Data set S1) and mapped onto the structure. The Fab41 footprints are outlined as in (A). (C) Location of the escape mutations A392E and G123D, which prevent neutralization by MAb #41 and MAb #47, respectively. (D) Close-up view of the interactions between the Fab41 HCDR3 (blue) and VP8*/VP5*. Heavy chain Trp109 inserts into a hydrophobic pocket. There are multiple hydrogen bonds (green) between main-chain groups of the antibody and VP5*. (E) Close-up view of the interaction between the Fab41 HCDR1 (blue) and the VP5* hydrophobic loop (orange). Trp393 of VP5* packs against the hydrophobic side of the Fab41 main chain and forms a hydrogen bond (green) with the side chain of Thr29. The side chain of Asn32 forms a hydrogen bond with the main chain carbonyl of Pro389. (F) Close-up view of the interactions between the Fab41 light chain (light blue) and one of the two VP8* domains (magenta). This part of the antibody-antigen interface involves mainly polar interactions.

within the Fab41 footprint (Fig. 3B), consistent with the heterotypic neutralization activity of MAb #41 (11). The mutation A392E in VP5* leads to escape from neutralization by MAb #41, but not by MAb #47 (11). A different mutation, G123D, at a position distant from residue 392, prevents neutralization by MAb #47, but not by MAb #41. The structure is consistent with these observations: VP5* A392 is in the middle of the Fab41 heavy-chain binding interface, while VP8* G123 does not contact Fab41 at all (Fig. 3C). Mutating alanine 392 to glutamic acid would disrupt hydrophobic contacts between VP5* and Fab41.

The most extensive set of interactions of MAb #41 is with its 18-residue long heavy-chain complementarity determining region 3 (HCDR3), which inserts laterally into the crevice bounded by the two VP8* chains and two of the VP5* hydrophobic loops, making both polar and nonpolar contacts (Fig. 2 and 3D). The heavy chain CDR1 (HCDR1) also contacts VP5*, clamping the loop from residues 386 to 394 between it and HCDR3 (Fig. 3E). The interaction includes hydrogen bonds between heavy-chain Thr29 and VP5* Trp393 in VP5*, with the latter also stacked onto a main-chain segment of HCDR1, and between the side chain of Asn32, in HCDR1, and the main-chain carbonyl of Pro389 in VP5* (Fig. 3E). Light chain contacts are almost exclusively with the VP8* opposite to the noncontacted VP5* (Fig. 3F).

Antibody 41 (p111w109) derives from the same germ line precursor as two others from the same donor (Fig. S4 in the supplemental material). We used the Clonalyst software (14, 15) to construct the most probable clonal lineage and in particular to infer the sequence of the unmutated common ancestor of the three B cell antigen receptor (BCR) sequences. Between 22 and 24 nonsilent somatic mutations (both chains, including the most probable HCDR3 mutations) are present in each of the three identified variable domains, indicating that the precursors of the corresponding B cells had undergone more than one round of affinity maturation—fully consistent with the likely history of adult donors. The highlighted mutations in Fig. S4 create polar interactions with VP8* or VP5*, suggesting that at least some of the previous exposure was to other P[8] viruses—consistent with the history of P[8] as the major circulating human rotavirus genotype.

Amino-acid differences between P12 and P45. The passage 28 (P28) and 45 (P45) CDC-9 viruses, grown in Vero cells after passage 13, have markedly higher infectivity in Caco-2 and Vero cells than does the P12 virus, grown in MA104 cells, which is identical in its entire genome sequence to the original isolate. The P45 virus acquired six amino-acid mutations in VP4 during the intervening rounds of virus passaging in Vero cells (one in VP8* and the others in VP5*) (Fig. 4A and B), all but one of which were already present in P28. After specimen preparation, the VP8*/VP5* spikes on the P12 particles were either in the post-entry, reversed conformation or in an intermediate conformation in which the foot remained anchored in the particle, but the VP8* lectin domains and the VP5* β -barrel domains were disordered. Thus, essentially all the spikes had rearranged or begun to rearrange from their upright conformation. In the P45 particles, nearly half the spikes were still upright, and we could therefore infer that one or more of the mutations during passage had altered the relative stabilities of upright and reversed conformations, in favor of the former.

One of the six mutations, S331F, at the apex of VP5*, introduced a phenylalanine side chain that packs into a hydrophobic pocket bounded by residues on the paired subunit: Gly67, Pro68 and Tyr69 on VP8* and its counterpart, Phe331, on VP5* (Fig. 4C). We suggest that the resulting well-packed, hydrophobic interface is the primary contributor to persistence of the upright conformation in the P45 virus. A larger fraction of spikes in that conformation, which is the functional starting point for attachment and penetration, should enhance infectivity in cell culture, as observed.

DISCUSSION

Our previous work on stages of rotavirus entry has led us to distinguish the following steps: attachment, engulfment, membrane perforation, release of VP7 and VP8*/VP5* from

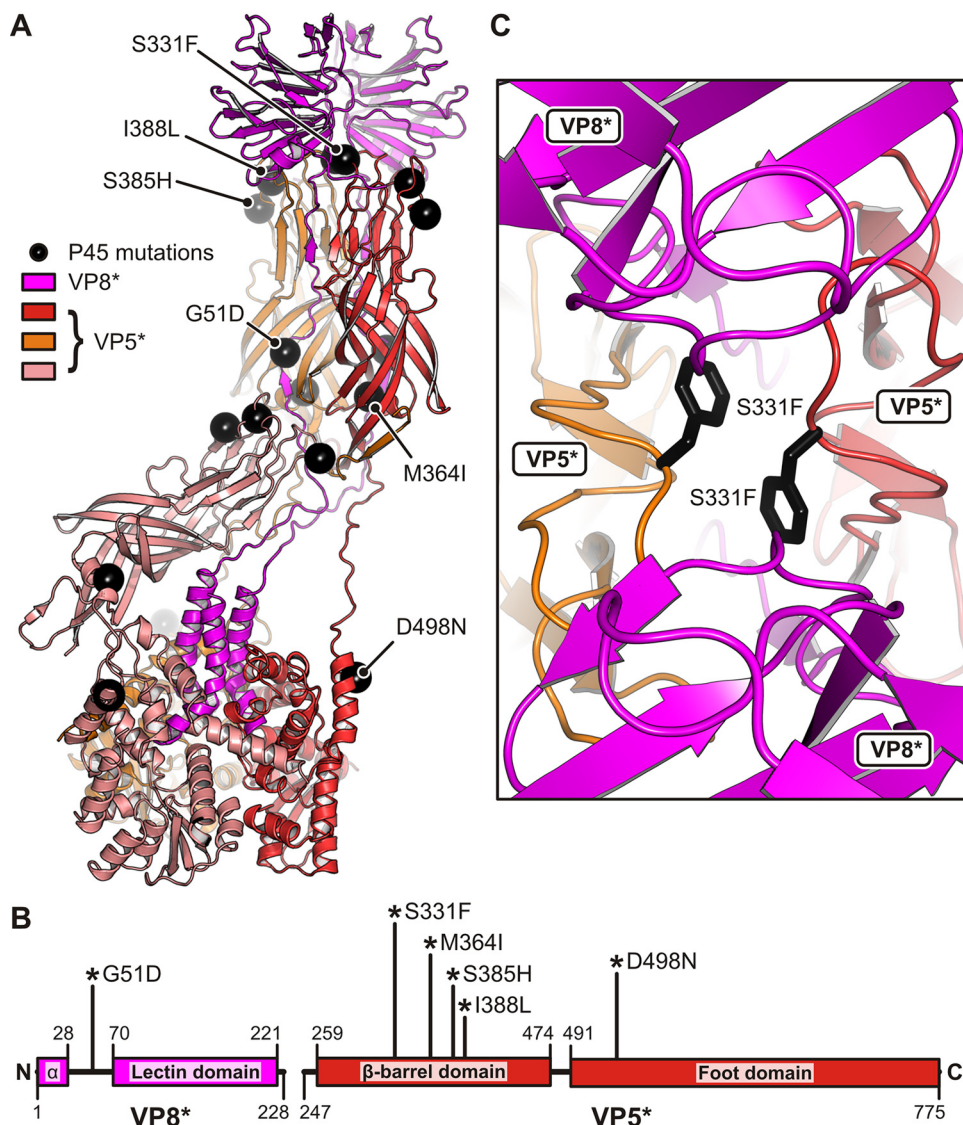


FIG 4 Human rotavirus CDC-9 strain P45 mutations mapped onto the VP8*/VP5* structure. (A) Mutations are shown as black spheres mapped onto the structure of the upright spike. (B) Primary structure diagram of VP8* and VP5*. Residue numbers corresponding to domain boundaries are shown. The positions of mutations observed in P45 are shown on top. Mutations at amino acid position 51, 331, 364, 385, and 388 occurred between passages 12 and 27 in Vero cells. Mutation at amino acid position 499 occurred between passages 28 and 43. (C) Close-up view of the S331F mutation at the dimeric interface of the VP5* tips.

an endocytic compartment into the cytosol, and release of the DLP (5). In BSC-1 cells, the endocytic compartment appears to be a vesicle generated not by a clathrin coat but by the TLP itself, which interacts tightly with the host-cell membrane through a pair of hydrophobic loops at the apex of the VP5* β -barrel domain (5). That interaction, as visualized directly by cryo-EM, can in principle be strong enough to wrap membrane fully around the virus particle (8). Initial attachment is through binding of the VP8* lectin domain with a glycan receptor, and excursions of that domain away from the VP5* hydrophobic loops would expose them for capture by the apposed vesicular membrane. In cells other than BSC-1, some fraction of the uptake might be through clathrin-coated vesicles, but as these uncoat immediately after pinching off (16–18), the outcome of either mode of engulfment would be the same. Penetration is thus from a small vesicle; larger endosomes (e.g., any with associated Rab5) are dead ends (5).

Binding of MAAb #41 covers the hydrophobic loops on VP5* and anchors both VP8* lectin domains. It does not block known sites for attachment to human glycan

receptors, but it would inhibit any stochastic excursions of the VP8* lectin domains away from the VP5* hydrophobic loops and would therefore inhibit any membrane interaction steps, including engulfment (unless driven by clathrin-mediated uptake) and membrane perforation. The structure of the Fab complex is also consistent with the heterotypic neutralization potency of this antibody as previously characterized (11). The residues contacted on the CDC-9 P1A[8] VP8* and VP5* are conserved in other P[8] spikes and conserved or conservatively mutated on most P[4] spikes (Data set S1 in the supplemental material); inspection of the model suggests that the P[4] spike differences would not interfere with binding of antibody 41 in the mode shown by our structure. The substitution D334H in the ST3 human P2A[6] isolate would probably conflict sterically with the HCDR3 loop of Fab41. Likewise, the escape mutation, A392E (in one of the hydrophobic loops), selected in the Wa P[8] strain for resistance to CDC-9, would clash with HCDR1 (11).

Perforation requires the VP5* conformational transition shown in Fig. 1D and E and in particular extrusion of the VP5* foot domain and its insertion into the membrane of the surrounding vesicle. The reversed conformation will therefore be inactive, or nearly so, in mediating infectious entry, because the transition will already be complete. On the virus after 12 passages of the original isolate, nearly all the spikes were in the reversed conformation in our prepared specimens and the *in vitro* infectivity was correspondingly very low. Presumably *in vivo*, the time from virus release to spike reversal is longer than the transfer time to infect a new intestinal cell, and the initial isolate and the P12 virus are both fully infectious in neonatal rats. On the attenuated, P45 virus, which had gained *in vitro* infectivity in the course of Vero-cell passaging, many of the spikes were still upright and hence in the correct starting conformation for infectious entry.

All but one of the six mutations in VP4 that occurred during the repeating passaging are in the VP5* fragment. The only one of the six that stands out as a likely cause of enhanced stability of the upright conformation is S331F (Fig. 4C). The contacts of the bulky phenyl side chain would probably reduce the frequency of any transient dissociation of the VP8* lectin domain from the apex of the paired, projecting VP5* β -barrel domains and would hence maintain the infectious spike conformation longer than on the initial CDC-9 isolate. This proposed effect of the S331F mutation is also consistent with the postulated spontaneous dissociation of the VP8* lectin domain from the hydrophobic loops of VP5*, allowing the loops to engage the target membrane and thereby prevent re-docking of the lectin domain. Because of the tight association of the N-terminal, 14-residue segment of VP8* with the VP5* foot, which tethers VP8* to the VP5* assembly, dissociation of the lectin domain from the VP5* apex would not release the particle from attachment with the surrounding membrane and, in the event of failure of the loops to engage the lipid bilayer, would allow the lectin domain to “snap back” onto VP5* rather than dissociate completely.

Mutations at VP4 positions 51, 331, and 385 are present in other attenuated strains. The Rotarix vaccine strain has mutations at all three (19, 20), and an attenuated strain of the Wa human isolate has mutations at 51 and 385 (21). Changes at 385, which is close to the membrane-interacting, hydrophobic loops in VP5*, are also prevalent in another systematic study of serial passaging in cell culture (22). The residue lies just outside the footprint of MAb #41. The consistent occurrence of mutations at position 385 is striking, but whether this or any of the VP4 mutations can account for attenuation *in vivo* of CDC-9 will depend on potential differences in the kinetics of infection in the gut and in cell culture and on the pathway(s) of initial engulfment and uptake. Moreover, attenuation *in vivo* could instead occur at other steps in the infectious cycle, including any of the stages of particle assembly. Although DLPs assemble in cytosolic viral “factories,” they must associate with VP4 and NSP4—the viral maturation receptor on the endoplasmic reticulum (ER)—and then acquire the VP7 glycoprotein in the ER lumen, by a still ill-characterized, concerted inward budding (23–25). Any of the VP4 mutations could in principle reduce the rate or efficiency of this multistep process.

MATERIALS AND METHODS

Virus production and purification. CDC-9 was isolated in the United States from a child hospitalized with diarrhea. The virus was initially adapted for seven passages (P7) in MA104 cells followed by passaging in Vero cells up to passage 45 (P45). In this study, we analyzed CDC-9 P12 (passaged 5 more times from P7 in MA104 cells) and CDC-9 P45 (passaged in Vero cells from P7 to P45). CDC-9 has no sequence changes from stool to P12 in MA104 cells, but has some mutations, primarily in VP4 gene, when adapted to grow in Vero cells (4). Viruses were cultivated and purified as previously described (3). Briefly, virus cultures were harvested at day 4–5 postinfection by freeze-thawing. Supernatants were clarified by centrifugation at 9800 g for 30 min. Cellular lipids were removed from the preparation by using a sucrose cushion. TLPs were purified by CsCl gradient ultracentrifugation, washed by centrifugation at 105,000 g for 2 h, and suspended in Hanks Balanced Salt Solution with Ca^{2+} (ThermoFisher, cat #14025092).

Fab expression and purification. hRV41 variable heavy and light sequences were synthesized as gBlock Gene Fragments by IDT and codons were optimized using IDT's Codon Optimization Tool for the organism *Homo sapiens* (human). These DNA sequences were subcloned using restriction enzymes NheI and KsaI into pVRC8400 vectors containing the human constant heavy and light chain regions and a tissue plasminogen activator signal sequence; the heavy-chain plasmid had a noncleavable 6 \times His tag (26). Plasmids were sequence-confirmed by the Dana Farber Sequencing Core. The Fab was transiently expressed in mammalian HEK 293 cells using Lipofectamine 2000 (Invitrogen) and 25 μg of total DNA (12.5 μg of each plasmid) following manufacturer's protocol for transfection reagent amount and cell density (26). Supernatants were harvested 5 days posttransfection and passed over Cobalt-TALON resin (TaKaRa) followed by size exclusion chromatography on Superdex 200 Increase 10/300 GL (GE Healthcare) in PBS. Purity was assessed by SDS-PAGE analysis.

Specimen preparation and cryo-EM data collection. We applied 3.5 μL purified CDC-9 rotavirus with Fab41 (~ 2.1 mg/mL, P12 data set; ~ 2.1 mg/mL, P45 data set 1; ~ 3.5 mg/mL, P45 data set 2) onto a glow-discharged, 400-mesh copper Quantifoil R1.2/1.3 holey carbon grid. Grids were blotted for 7–8 s at 100% relative humidity and flash-frozen in liquid nitrogen-cooled liquid ethane using an FEI Vitrobot Mark I. Grids were then loaded onto an TF30 Polara electron microscope operating at 300 kV accelerating voltage. Movie image stacks were recorded on a Gatan K2 Summit direct detector set in super-resolution counting mode at the calibrated magnification of $\times 40617$ using SerialEM (27), with a defocus range between -1.0 and -3.5 μm . This gives a pixel size of 1.231 \AA at the image plane. The electron dose rate was set to 8 per physical pixel per second and the exposure time 200 ms per frame. Total exposure times were 7 s (P12 data set), 13 s (P45 data set 1), and 10 s (P45 data set 2), resulting in 35, 65, and 50, frames per movie stack, respectively. The total electron doses were 37.0, 68.7, and 52.9 electrons per \AA^2 (~ 1.1 electrons per \AA^2 per frame) for these three different samples, respectively.

Cryo-EM data processing. (i) Movie processing and icosahedral reconstructions. We used MotionCor2 (28) with 5×5 patch alignment to calculate summed micrographs from the movie frames. With Gautomatch we picked viral particles based on template projections (3° angular sampling, low-pass-filtered with a spatial frequency cutoff corresponding to 40 \AA resolution) obtained with EMAN2 (29) from a previous RRV reconstruction (30). Contrast transfer function (CTF) parameters were estimated using Gctf (31) from total-summed micrographs. CTF values were locally refined at particle positions. We used relion_preprocess (32) for particle extraction and normalization (box size of 1024×1024 pixels). We obtained initial icosahedral reconstructions (l2 setting) with cisTEM (33) (refine3d version 1.01, reconstruct3d version 1.02). The 3D reference was masked with a spherical shell mask that had an inner radius of 222 \AA and an outer radius of 403 \AA . At this stage, we excluded false-positive particle picks and DLP particles, as evident from low alignment scores, from the stack (Table 1 and Fig. S1). The alignment resolution limit was initially 12 \AA for the global angular search and later extended to 4 \AA during local refinement. We used relion_motion_refine to further refine movie frame alignment and determine optimal weighting factors for frame summation, and relion_ctf_refine (34) to estimate beam-tilt correction parameters. After another round of alignment in cisTEM and reconstruction of maps with relion_reconstruct, the Fourier shell correlations (FSCs) calculated for density within the volume of the spherical shell mask were 3.5 \AA (P12 data set), 3.2 \AA (P45 Data set 1), and 3.2 \AA (P45 Data set 2) (Table S1 in the supplemental material).

(ii) Local reconstructions. We obtained local reconstructions centered at VP4 (VP5* and VP8*) positions using subparticle image analysis and classification as previously described (8). Based on the icosahedral alignment, we calculated for each of the 60 VP4 protomers a subparticle extraction position and new alignment angles and shifts for projection on protomer 1 of the extracted subparticle using Python scripting with the library Transformations.py (<https://pypi.org/project/transformations>). We used IMOD (35) to prepare three subparticle stacks for each data set: (i) a signal-subtracted stack 1 with a box size of 264×264 pixels where we used relion_project to subtract all density except for VP4, Fab41, and a single VP7 trimer before subparticle extraction; (ii) a signal-subtracted stack 2 with a box size of 264×264 pixels where we subtracted all density except for the VP5* β -barrel domains, the VP8* domains, and the Fab41 before subparticle extraction; (iii) an original, nonsignal-subtracted stack 3 with a box size of 320×320 pixels.

We classified subparticles of stack 1 with the programs refine3d (version 1.01) and reconstruct3d (version 1.02) from cisTEM (33). We kept the alignment parameters constant during 60 cycles of iterative classification. The high-resolution limit for classification was 8 \AA , and particles were used in the reconstruction step indiscriminate of their alignment score by setting the BSC parameter to 0.0. During classification, we masked the 3D reference of all classes with the same mask encompassing potential VP4 spike volume of the upright and reversed conformations, and the region of the single VP7 trimer that was not signal-subtracted. We obtained essentially the same results from classifications where the initial 3D references for the different classes were

either prepared from random particle distributions or were seeded with known structures (Table 1). The reconstructions of the upright and reversed classes observed in the P45 data sets 1 and 2 had a very similar structure and resolution as previously reported for RRV (8) (Table S1 and Fig. S2A–F in the supplemental material). Final density maps for these two classes were calculated from the nonsignal-subtracted particle stack 3 obtained from the P45 data set 1, and post-processed with `sharpen_map` from `cisTEM`, where a B factor of -90 \AA^2 was applied at low resolution and average amplitudes were flattened between spatial frequencies corresponding to 8.0 and 3.2 \AA resolution.

(iii) Focused reconstruction of distal spike components. Because the two VP5* dimeric β -barrel domains were flexible with a hinge-point at their base, we could not interpret density belonging to the Fab41 antibodies in the upright spike class after subparticle classification (Fig. 1B). We were unsuccessful in directly focusing alignment using a mask that only covered this region for the 3D reference and using particle stack 2, where everything was signal-subtracted except the dimeric VP5* β -barrel domains, the VP8* domains, and the bound Fab41 antibodies. This approach probably failed because the starting 3D reference had an estimated resolution lower than 6 \AA , the molecular weight of the entity was too small, and overlapping density from the virus interior, other spikes, or imperfectly subtracted density from the viral shell prevented stable alignment and degraded the reconstruction. We therefore used an approach of alignment by classification (Fig. 1). For this we merged the upright-conformation particles of stack 3 from the P45 data sets 1 and 2 and used the `cisTEM` programs for classification with six classes and constant particle alignment parameters (60 cycles). The resolution limit for classification was 5 \AA . We next calculated new particle alignment parameters (ψ , θ , ϕ , dx , dy) based on transformation matrices calculated from structures (VP5* β -barrel domains, VP8* domains, and the Fab41 variable domains) that we had rigid-body fitted into the maps of the six classes. The new particle alignment parameters are equivalent to aligning the maps of the six classes in real space. After a total of three cycles, the alignment by classification algorithm had converged and the nominal resolution for this part 4.4 \AA (Fig. 1C). With the improved map as 3D reference, we used `cisTEM` for one round of alignment. We also used the CCP4 program `maprot` (36) for 2-fold local symmetry averaging. These steps led to nominal resolutions of 3.8 and 3.5 \AA , respectively (Fig. S2G and H in the supplemental material).

(iv) Composite map and resolution estimation. For structure refinement of the upright conformation model with bound Fab41 antibodies (see below), we prepared a composite map (Fig. 2B) by pasting together the well-resolved parts of the sub particle classification map (VP6, VP7, VP4 chains 1–3 without residues 33–482 of chains 1 and 2) and the final focused reconstruction map (VP4 residues 33–482 of chains 1 and 2, Fab41). Corresponding regions were masked before pasting together and, in case of overlap, grid points with the higher density value were selected for the composite map using `EMAN2`. We used `phenix.mtriage` (37) to calculate FSC curves from masked half maps (Table S1 and Fig. S2A–C, G) and estimated local resolutions with `reliion_postprocess` (Fig. S2D–F, H).

Model building and refinement. We used the basic protocol of `Modeller` (38) and the RRV structures (PDB-ID 6WXE, upright conformation; PDB-ID 6WVG, reversed conformation) (8) as templates to prepare homology models for the human rotavirus CDC-9 strain proteins VP6, VP7, and VP4 (VP5* and VP8*). The antibody Fab41 heavy and light chains were modeled based on PDB-ID 6PHC chain A (87% sequence identity) (39) and PDB-ID 6MG4 chain A (91% sequence identity) (40), respectively. All homology models, except the constant domains of the Fab41 heavy and light chains (residues 127–231 and 113–218, respectively), were then fitted into the composite density maps by rigid-body refinement, morphing, simulated annealing, and global and local refinement as implemented in `phenix.real_space_refine` (41). After the initial fit, we manually checked the models in O and made adjustments where necessary. We also built N-linked glycans at VP7 residues Asn69 and Asn238, added four Ca^{2+} ions per VP7 protomer, and placed the Fab41 heavy and light chain domains as rigid-bodies based on density as observed in low-pass filtered maps. After these adjustments, we refined the models again by global, local, and B factor refinement. In addition to standard stereochemical and B factor restraints, we also used rotamer, Ramachandran, and secondary structure restraints in the refinement target function. The Fab41 heavy and light chain are flexible with respect to the variable domains and thus poorly resolved in our reconstruction. We therefore used reference model restraints for these domains during refinement, which essentially maintained their structure as obtained from `Modeller`. Modeled residues of the upright and reversed structures are listed in Table S2. We validated the stereochemistry of the structures with `MolProbity` (42) (Table S1 in the supplemental material) and assessed their fit to the cryo-EM reconstructions with `phenix.mtriage` (37) (Fig. S2). We also validated the stereochemical conformation of the modeled N-linked glycans with `Privateer` (43). Modeled residues are summarized in Table S2.

Sequence alignments. We retrieved rotavirus amino acid sequences for VP4 (Data set S1 in the supplemental material), VP7 (Data set S2), and VP6 (Data set S3) from UniProt (44) using `BioPython` (45) and aligned them with `MAFFT` (46). VP4 accession numbers are as follows: WA, P11193; WI61, B3SRX5; S2, AQT31697; DS-1, P11196; L26, P21284; ST3, P11200; AU-1, P39033; 69M, P26451; NDCV, P17465; OSU, P11114; SA11, P12976; RRV, P12473. VP7 accession numbers are as follows: WA, P03532; WI61, B3SRX9; S2, P04510; DS-1, P11850; L26, P21285; ST3, P10501; AU-1, O42044; 69M, B3SRQ7; NDCV, P04511; OSU, P08406; SA11, P03533; RRV, P12476. VP6 accession numbers are as follows: WA, P03530; WI61, B1NKU4; S2, P08035; DS-1, A7J3A8; L26, B1NKS8; ST3, B1NKU0; AU-1, A4ZCW7; 69M, B1NKQ8; NDCV, A7J3A1; OSU, Q91N61; SA11, P03531; RRV, B2BN53. Serotypes and genotypes for the different strains were compiled from published studies (47–50) and `ViralZone` (51).

Figure preparation. We prepared the figures using `PyMol` (The PyMOL Molecular Graphics System, Version 2.3 Schrödinger, LLC), `POV-Ray` (www.povray.org), and `matplotlib` (52). We made the sequence alignment figures (Data set S1–3 in the supplemental material) with `ESPrInt` (53). To calculate the conservation shown in Fig. 3B, we obtained positional conservation scores from the multiple sequence alignment (Data set S1) and generated a coordinate file for the figure with the program `ConSurf` (54).

Data availability. The cryo-EM maps can be obtained from the Electron Microscopy Data Bank (accession identifier [EMD-26608](https://www.ebi.ac.uk/emdb/EMD-26608), upright conformation with bound Fab41; [EMD-26609](https://www.ebi.ac.uk/emdb/EMD-26609), reversed conformation) and the atomic coordinates from the Protein Data Bank (accession identifier PDB-ID [7UMS](https://www.rcsb.org/entry/7UMS), upright conformation with bound Fab41; PDB-ID [7UMT](https://www.rcsb.org/entry/7UMT), reversed conformation).

SUPPLEMENTAL MATERIAL

Supplemental material is available online only.

SUPPLEMENTAL FILE 1, PDF file, 1.2 MB.

ACKNOWLEDGMENTS

We thank the staff of the Harvard Medical School Molecular Electron Microscopy Suite. The research was supported by NIH grants CA13202 (to S.C.H.), AI125249 (to H.B.G.), and VA Merit Grant GRH0022 (to H.B.G.). S.C.H. is an Investigator in the Howard Hughes Medical Institute.

The findings and conclusions in this article are those of the authors and do not necessarily represent the Centers for Disease Control and Prevention (CDC).

REFERENCES

- Desselberger U. 2017. Differences of rotavirus vaccine effectiveness by country: likely causes and contributing factors. *Pathogens* 6:65. <https://doi.org/10.3390/pathogens6040065>.
- Parker EP, Ramani S, Lopman BA, Church JA, Iturriza-Gomara M, Prendergast AJ, Grassly NC. 2018. Causes of impaired oral vaccine efficacy in developing countries. *Future Microbiol* 13:97–118. <https://doi.org/10.2217/fmb-2017-0128>.
- Esona MD, Foytich K, Wang Y, Shin G, Wei G, Gentsch JR, Glass RI, Jiang B. 2010. Molecular characterization of human rotavirus vaccine strain CDC-9 during sequential passages in Vero cells. *Hum Vaccin* 6:10409.
- Resch TK, Wang Y, Moon S, Jiang B. 2020. Serial passaging of the human rotavirus CDC-9 strain in cell culture leads to attenuation: characterization from in vitro and in vivo studies. *J Virol* 94:e00889-20. <https://doi.org/10.1128/JVI.00889-20>.
- Abdelhakim AH, Salgado EN, Fu X, Pasham M, Nicastro D, Kirchhausen T, Harrison SC. 2014. Structural correlates of rotavirus cell entry. *PLoS Pathog* 10:e1004355. <https://doi.org/10.1371/journal.ppat.1004355>.
- Salgado EN, Garcia Rodriguez B, Narayanaswamy N, Krishnan Y, Harrison SC. 2018. Visualization of calcium ion loss from rotavirus during cell entry. *J Virol* 92:e01327. <https://doi.org/10.1128/JVI.01327-18>.
- Salgado EN, Upadhyayula S, Harrison SC. 2017. Single-particle detection of transcription following rotavirus entry. *J Virol* 91. <https://doi.org/10.1128/JVI.00651-17>.
- Herrmann T, Torres R, Salgado EN, Berciu C, Stoddard D, Nicastro D, Jenni S, Harrison SC. 2021. Functional refolding of the penetration protein on a non-enveloped virus. *Nature* 590:666–670. <https://doi.org/10.1038/s41586-020-03124-4>.
- De Vos B, Han HH, Bouckennooghe A, Debrus S, Gillard P, Ward R, Cheuvart B. 2009. Live attenuated human rotavirus vaccine, RIX4414, provides clinical protection in infants against rotavirus strains with and without shared G and P genotypes: integrated analysis of randomized controlled trials. *Pediatr Infect Dis J* 28:261–266. <https://doi.org/10.1097/INF.0b013e3181907177>.
- Velazquez FR, Matson DO, Calva JJ, Guerrero L, Morrow AL, Carter-Campbell S, Glass RI, Estes MK, Pickering LK, Ruiz-Palacios GM. 1996. Rotavirus infection in infants as protection against subsequent infections. *N Engl J Med* 335:1022–1028. <https://doi.org/10.1056/NEJM199610033351404>.
- Nair N, Feng N, Blum LK, Sanyal M, Ding S, Jiang B, Sen A, Morton JM, He XS, Robinson WH, Greenberg HB. 2017. VP4- and VP7-specific antibodies mediate heterotypic immunity to rotavirus in humans. *Sci Transl Med* 9:eaam5434. <https://doi.org/10.1126/scitranslmed.aam5434>.
- Settembre EC, Chen JZ, Dormitzer PR, Grigorieff N, Harrison SC. 2011. Atomic model of an infectious rotavirus particle. *EMBO J* 30:408–416. <https://doi.org/10.1038/emboj.2010.322>.
- Aoki ST, Settembre EC, Trask SD, Greenberg HB, Harrison SC, Dormitzer PR. 2009. Structure of rotavirus outer-layer protein VP7 bound with a neutralizing Fab. *Science* 324:1444–1447. <https://doi.org/10.1126/science.1170481>.
- Kepler TB. 2013. Reconstructing a B-cell clonal lineage. I. Statistical inference of unobserved ancestors. *F1000Res* 2:103. <https://doi.org/10.12688/f1000research.2-103.v1>.
- Kepler TB, Munshaw S, Wiehe K, Zhang R, Yu JS, Woods CW, Denny TN, Tomaras GD, Alam SM, Moody MA, Kelsoe G, Liao HX, Haynes BF. 2014. Reconstructing a B-Cell clonal lineage. II. Mutation, selection, and affinity maturation. *Front Immunol* 5:170. <https://doi.org/10.3389/fimmu.2014.00170>.
- Merrifield CJ, Feldman ME, Wan L, Almers W. 2002. Imaging actin and dynamin recruitment during invagination of single clathrin-coated pits. *Nat Cell Biol* 4:691–698. <https://doi.org/10.1038/ncb837>.
- Ehrlich M, Boll W, Van Oijen A, Hariharan R, Chandran K, Nibert ML, Kirchhausen T. 2004. Endocytosis by random initiation and stabilization of clathrin-coated pits. *Cell* 118:591–605. <https://doi.org/10.1016/j.cell.2004.08.017>.
- Massol RH, Boll W, Griffin AM, Kirchhausen T. 2006. A burst of auxilin recruitment determines the onset of clathrin-coated vesicle uncoating. *Proc Natl Acad Sci U S A* 103:10265–10270. <https://doi.org/10.1073/pnas.0603369103>.
- Ward RL, Kirkwood CD, Sander DS, Smith VE, Shao M, Bean JA, Sack DA, Bernstein DI. 2006. Reductions in cross-neutralizing antibody responses in infants after attenuation of the human rotavirus vaccine candidate 89–12. *J Infect Dis* 194:1729–1736. <https://doi.org/10.1086/509623>.
- Ward RL, Bernstein DI. 2009. Rotarix: a rotavirus vaccine for the world. *Clin Infect Dis* 48:222–228. <https://doi.org/10.1086/595702>.
- Guo Y, Wentworth DE, Stucker KM, Halpin RA, Lam HC, Marthaler D, Saif LJ, Vlasova AN. 2020. Amino acid substitutions in positions 385 and 393 of the hydrophobic region of VP4 may be associated with rotavirus attenuation and cell culture adaptation. *Viruses* 12:408. <https://doi.org/10.3390/v12040408>.
- Tsugawa T, Tsutsumi H. 2016. Genomic changes detected after serial passages in cell culture of virulent human G1P[8] rotaviruses. *Infect Genet Evol* 45:6–10. <https://doi.org/10.1016/j.meegid.2016.08.015>.
- Trask SD, McDonald SM, Patton JT. 2012. Structural insights into the coupling of virion assembly and rotavirus replication. *Nat Rev Microbiol* 10:165–177. <https://doi.org/10.1038/nrmicro2673>.
- Altenburg BC, Graham DY, Estes MK. 1980. Ultrastructural study of rotavirus replication in cultured cells. *J Gen Virol* 46:75–85. <https://doi.org/10.1099/0022-1317-46-1-75>.
- Poruchynsky MS, Tyndall C, Both GW, Sato F, Bellamy AR, Atkinson PH. 1985. Deletions into an NH2-terminal hydrophobic domain result in secretion of rotavirus VP7, a resident endoplasmic reticulum membrane glycoprotein. *J Cell Biol* 101:2199–2209. <https://doi.org/10.1083/jcb.101.6.2199>.
- Schmidt AG, Xu H, Khan AR, O'Donnell T, Khurana S, King LR, Manischewitz J, Golding H, Suphaphiphat P, Carfi A, Settembre EC, Dormitzer PR, Kepler TB, Zhang R, Moody MA, Haynes BF, Liao HX, Shaw DE, Harrison SC. 2013. Pre-configuration of the antigen-binding site during affinity maturation of a broadly neutralizing influenza virus antibody. *Proc Natl Acad Sci U S A* 110:264–269. <https://doi.org/10.1073/pnas.1218256110>.
- Mastrorade DN. 2005. Automated electron microscope tomography using robust prediction of specimen movements. *J Struct Biol* 152:36–51. <https://doi.org/10.1016/j.jsb.2005.07.007>.
- Zheng SQ, Palovcak E, Armache JP, Verba KA, Cheng Y, Agard DA. 2017. MotionCor2: anisotropic correction of beam-induced motion for improved cryo-electron microscopy. *Nat Methods* 14:331–332. <https://doi.org/10.1038/nmeth.4193>.

29. Tang G, Peng L, Baldwin PR, Mann DS, Jiang W, Rees I, Ludtke SJ. 2007. EMAN2: an extensible image processing suite for electron microscopy. *J Struct Biol* 157:38–46. <https://doi.org/10.1016/j.jsb.2006.05.009>.
30. Jenni S, Salgado EN, Herrmann T, Li Z, Grant T, Grigorieff N, Trapani S, Estrozi LF, Harrison SC. 2019. In situ structure of rotavirus VP1 RNA-dependent RNA polymerase. *J Mol Biol* 431:3124–3138. <https://doi.org/10.1016/j.jmb.2019.06.016>.
31. Zhang K. 2016. Gctf: Real-time CTF determination and correction. *J Struct Biol* 193:1–12. <https://doi.org/10.1016/j.jsb.2015.11.003>.
32. Scheres SH. 2012. RELION: implementation of a Bayesian approach to cryo-EM structure determination. *J Struct Biol* 180:519–530. <https://doi.org/10.1016/j.jsb.2012.09.006>.
33. Grant T, Rohou A, Grigorieff N. 2018. cisTEM, user-friendly software for single-particle image processing. *Elife* 7:e35383. <https://doi.org/10.7554/eLife.35383>.
34. Scheres SH. 2014. Beam-induced motion correction for sub-megadalton cryo-EM particles. *Elife* 3:e03665. <https://doi.org/10.7554/eLife.03665>.
35. Mastronarde DN, Held SR. 2017. Automated tilt series alignment and tomographic reconstruction in IMOD. *J Struct Biol* 197:102–113. <https://doi.org/10.1016/j.jsb.2016.07.011>.
36. Winn MD, Ballard CC, Cowtan KD, Dodson EJ, Emsley P, Evans PR, Keegan RM, Krissinel EB, Leslie AG, McCoy A, McNicholas SJ, Murshudov GN, Pannu NS, Potterton EA, Powell HR, Read RJ, Vagin A, Wilson KS. 2011. Overview of the CCP4 suite and current developments. *Acta Crystallogr D Biol Crystallogr* 67:235–242. <https://doi.org/10.1107/S0907444910045749>.
37. Afonine PV. 2017. phenix.mtriage: a tool for analysis and validation of cryo-EM 3D reconstructions. *Computational Crystallography Newsletter* 8:25.
38. Webb B, Sali A. 2016. Comparative protein structure modeling using MODELLER. *Curr Protoc Protein Sci* 86:2.9.1–2.9.37. <https://currentprotocols.onlinelibrary.wiley.com/doi/10.1002/cpps.20>.
39. McLeod B, Miura K, Scally SW, Bosch A, Nguyen N, Shin H, Kim D, Volkmuth W, Ramisch S, Chichester JA, Streatfield S, Woods C, Schief WR, Emerling D, King CR, Julien JP. 2019. Potent antibody lineage against malaria transmission elicited by human vaccination with Pfs25. *Nat Commun* 10:4328. <https://doi.org/10.1038/s41467-019-11980-6>.
40. Morgan GJ, Yan NL, Mortenson DE, Rennella E, Blundon JM, Gwin RM, Lin CY, Stanfield RL, Brown SJ, Rosen H, Spicer TP, Fernandez-Vega V, Merlini G, Kay LE, Wilson IA, Kelly JW. 2019. Stabilization of amyloidogenic immunoglobulin light chains by small molecules. *Proc Natl Acad Sci U S A* 116:8360–8369. <https://doi.org/10.1073/pnas.1817567116>.
41. Afonine PV, Poon BK, Read RJ, Sobolev OV, Terwilliger TC, Urzhumtsev A, Adams PD. 2018. Real-space refinement in PHENIX for cryo-EM and crystallography. *Acta Crystallogr D Struct Biol* 74:531–544. <https://doi.org/10.1107/S2059798318006551>.
42. Chen VB, Arendall WB, 3rd, Headd JJ, Keedy DA, Immormino RM, Kapral GJ, Murray LW, Richardson JS, Richardson DC. 2010. MolProbity: all-atom structure validation for macromolecular crystallography. *Acta Crystallogr D Biol Crystallogr* 66:12–21. <https://doi.org/10.1107/S0907444909042073>.
43. Agirre J, Iglesias-Fernandez J, Rovira C, Davies GJ, Wilson KS, Cowtan KD. 2015. Privateer: software for the conformational validation of carbohydrate structures. *Nat Struct Mol Biol* 22:833–834. <https://doi.org/10.1038/nsmb.3115>.
44. UniProt C. 2019. UniProt: a worldwide hub of protein knowledge. *Nucleic Acids Res* 47:D506–D515. <https://doi.org/10.1093/nar/gky1049>.
45. Cock PJ, Antao T, Chang JT, Chapman BA, Cox CJ, Dalke A, Friedberg I, Hamelryck T, Kauff F, Wilczynski B, de Hoon MJ. 2009. Biopython: freely available Python tools for computational molecular biology and bioinformatics. *Bioinformatics* 25:1422–1423. <https://doi.org/10.1093/bioinformatics/btp163>.
46. Katoh K, Misawa K, Kuma K, Miyata T. 2002. MAFFT: a novel method for rapid multiple sequence alignment based on fast Fourier transform. *Nucleic Acids Res* 30:3059–3066. <https://doi.org/10.1093/nar/gkf436>.
47. Gorziglia M, Larralde G, Kapikian AZ, Chanock RM. 1990. Antigenic relationships among human rotaviruses as determined by outer capsid protein VP4. *Proc Natl Acad Sci U S A* 87:7155–7159. <https://doi.org/10.1073/pnas.87.18.7155>.
48. Martella V, Ciarlet M, Pratelli A, Arista S, Terio V, Elia G, Cavalli A, Gentile M, Decaro N, Greco G, Cafiero MA, Tempesta M, Buonavoglia C. 2003. Molecular analysis of the VP7, VP4, VP6, NSP4, and NSP5/6 genes of a buffalo rotavirus strain: identification of the rare P[3] rhesus rotavirus-like VP4 gene allele. *J Clin Microbiol* 41:5665–5675. <https://doi.org/10.1128/JCM.41.12.5665-5675.2003>.
49. Matthijnsens J, Ciarlet M, Heiman E, Arijis I, Delbeke T, McDonald SM, Palombo EA, Iturriza-Gomara M, Maes P, Patton JT, Rahman M, Van Ranst M. 2008. Full genome-based classification of rotaviruses reveals a common origin between human Wa-Like and porcine rotavirus strains and human DS-1-like and bovine rotavirus strains. *J Virol* 82:3204–3219. <https://doi.org/10.1128/JVI.02257-07>.
50. Patton JT. 2012. Rotavirus diversity and evolution in the post-vaccine world. *Discov Med* 13:85–97.
51. Hulo C, de Castro E, Masson P, Bougueleret L, Bairoch A, Xenarios I, Le Mercier P. 2011. ViralZone: a knowledge resource to understand virus diversity. *Nucleic Acids Res* 39:D576–82. <https://doi.org/10.1093/nar/gkq901>.
52. Hunter JD. 2007. Matplotlib: a 2D graphics environment. *Comput Sci Eng* 9:90–95. <https://doi.org/10.1109/MCSE.2007.55>.
53. Gouet P, Courcelle E, Stuart DI, Metz F. 1999. ESPript: analysis of multiple sequence alignments in PostScript. *Bioinformatics* 15:305–308. <https://doi.org/10.1093/bioinformatics/15.4.305>.
54. Ashkenazy H, Abadi S, Martz E, Chay O, Mayrose I, Pupko T, Ben-Tal N. 2016. ConSurf 2016: an improved methodology to estimate and visualize evolutionary conservation in macromolecules. *Nucleic Acids Res* 44:W344–W350. <https://doi.org/10.1093/nar/gkw408>.